Energy & Environmental Science

ROYAL SOCIETY OF CHEMISTRY

PAPER

View Article Online
View Journal | View Issue

Cite this: *Energy Environ. Sci.*, 2025, **18**, 6260

Stepwise volatilization induced by nature-sourced volatile solid additives improving the efficiency and stability of perovskite solar cells†

Jeewon Park, [a] Seoyoung Kim,[a] Wonjun Kim,[a] Zhe Sun,[a] Byongkyu Lee[a] and Changduk Yang *[ab]

In contrast to the substantial efforts dedicated to additive engineering in the field of perovskite solar cells (PSCs), the exploration of volatile solid additives has received surprisingly little attention. This study introduces a novel approach for fabricating highly efficient and stable PSCs by employing "naturally sourced volatile solid additives" (CP and CQ), which exhibit distinct volatilization rates and varying degrees of Lewis base–acid interactions with perovskite. During the PSC fabrication process involving two-stage thermal annealing, CP completely volatilized after the initial annealing step, resulting in the formation of a densely packed PbI_2 film. Conversely, owing to its robust Lewis base–acid interaction with perovskite through bidentate coordination, a certain amount of CQ tends to persist after the first annealing step. However, no residue was observed after the second annealing step (stepwise-volatilization mechanism). This process yields high-quality FA-based perovskite crystallinity characterized by large-grained perovskite and highly preferred crystallite orientation. Consequently, CQ-based PSCs achieve a promising power conversion efficiency (PCE) of 25.00% (independently certified at 24.89%) with exceptional MPPT stability (PCE retention of 90.1% after 1000 h, ISOS-L-1). This study underscores the viability of the naturally sourced volatile solid additives for ecofriendly manufacturing of PSCs.

Received 28th August 2024,
Accepted 9th May 2025

DOI: 10.1039/d4ee03897e

rsc.li/ees

Broader context

Perovskite solar cells (PSCs) are a promising candidate for next-generation photovoltaics owing to their excellent optoelectronic properties. Despite the current drastic advancements in PSCs, various defects can emerge owing to precursor compositions and processing conditions inherent to solution processing and rapid perovskite film growth. To address these sticking points, extensive research efforts have been devoted to additive engineering by controlling the film formation of perovskite layers. However, in the field of perovskite solar cells, the investigation of volatile solid additives has been rarely utilized compared to organic optoelectronics. Moreover, there are not many reports on nature-sourced additives. Herein, we report naturally derived volatile solid additives, namely camphor (CP) and camphorquinone (CQ), which improve the efficiency and stability of PSCs. The work introduces a "stepwise volatilization" to explain the working mechanism of CQ volatile additives on perovskite crystallization. As a result, the CQ-based PSC achieved an enhanced PCE of 25.00% compared to the 23.20% efficiency of the control device. This study provides a novel strategy using volatile natural additives to improve the photovoltaic performance and stability of PSCs.

1. Introduction

Halide perovskites, characterized by the ABX_3 crystal structure (where A = methylammonium (MA), formamidinium (FA), or cesium (Cs), B = lead or tin cation, X = a halogen anion), garnered significant attention due to their exceptional photoelectric properties.[1–7] These properties include a high absorption coefficient ($\sim 10^5$), a small exciton binding energy of less than 100 meV, an extended diffusion length exceeding 1 μm, and a tunable bandgap spanning from 1.2 to over 3 eV.[8–14] Remarkable progress has been achieved in the field of perovskite solar cells (PSCs) in only a few years. The power conversion efficiency (PCE) reached 26.08% through a range of strategies, including the development of novel functional materials, engineering of device interfaces, compositional tuning, and control of crystallization kinetics.[15–19]

[a] *School of Energy and Chemical Engineering, Ulsan National Institute of Science and Technology (UNIST), 50 UNIST-gil, Ulju-gun, Ulsan, 44919, South Korea. E-mail: yang@unist.ac.kr*
[b] *Graduate School of Carbon Neutrality, Ulsan National Institute of Science and Technology (UNIST), 50 UNIST-gil, Ulju-gun, Ulsan, 44919, South Korea*

† Electronic supplementary information (ESI) available. See DOI: https://doi.org/10.1039/d4ee03897e

Despite the current rapid advancements and ongoing enhancements in PSCs, various defects can emerge owing to precursor compositions and processing conditions inherent to solution processing and rapid perovskite film growth. The introduction of additives (*e.g.*, salts, molecules, polymers, and nanoparticles) has the potential to influence perovskite crystallization, film formation, bulk or surface defect passivation, and interface optimization in terms of structure and energetics.[20–26] Consequently, extensive research efforts have been devoted to additive engineering to address these challenges by controlling the thermodynamics and growth kinetics of perovskite films.

Concurrently, in the organic electronics community, "volatile solid additives" have demonstrated their effectiveness in directly modulating active layer morphology, leading to improved characteristics in organic photovoltaics, including PCE, device stability, and reproducibility.[27–35] While the use of volatile solid additives has become a widely adopted approach for achieving high-performance organic photovoltaics, it has surprisingly received limited attention in perovskite-based systems. Therefore, there is a pressing need for further research within the PSC community to explore volatile solid additives. This endeavor aims to develop advanced additive-related protocols and gain deeper insights into the underlying mechanisms governing the use of volatile solid additives.

In this study, we introduced naturally sourced volatile solid additives, namely camphor (CP) and camphorquinone (CQ), into the fabrication process of perovskite solar cells (PSCs). The PSCs were produced using a two-step sequential deposition technique that involved a two-stage thermal-annealing process.[36–40] Both CP and CQ are polar Lewis-base molecules containing carbonyl groups, but they differ in the number of carbonyl groups (Fig. 1a for their structures). This distinction gives rise to varying rates of volatilization and different degrees of Lewis base–acid interaction with the perovskite material.

Following the initial annealing step at 70 °C, CP molecules were entirely volatilized from the PbI_2 precursor, resulting in the formation of a tightly packed PbI_2 film. In contrast, some CQ molecules remained within the PbI_2 bulk film after the first annealing step. However, their complete volatilization occurred during the subsequent second annealing step at 150 °C, resulting in a stepwise-volatilization mechanism. This mechanism facilitated the development of high-quality FA-based perovskite crystallinity characterized by large-grained perovskite structures and a high degree of preferred crystallite orientation, enabling extremely high PCEs of 25.00% for a laboratory scale of 0.042 cm^2 (independently certified at 24.89%). Moreover, the operational stability of CQ-treated PSCs was considerably enhanced, which retained over 90.1% of the initial PCE after 1000 h under maximum power point tracking conditions (ISOS-L-1).

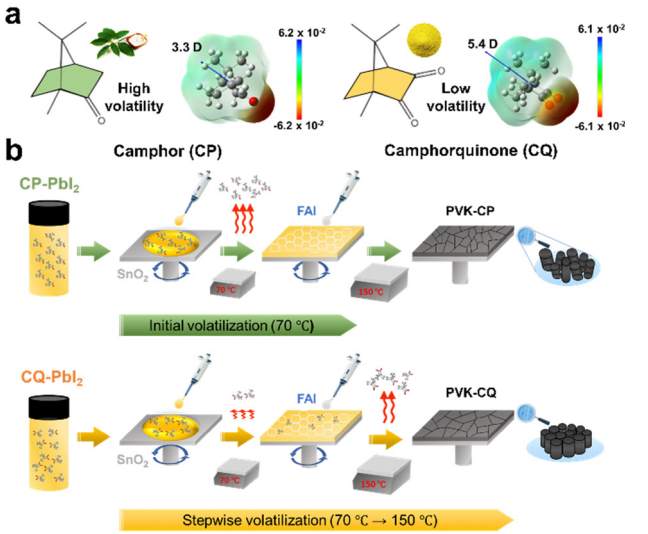

Fig. 1 Stepwise volatilization induced by volatile solid additives. (a) Chemical structures and electrostatic potential mappings of CP and CQ. (b) Schematic representation of the stepwise volatilization mechanism involving two-stage thermal annealing: an initial annealing at 70 °C for PbI_2 precursor and a second annealing step at 150 °C for perovskite (PVK) crystallization.

2. Results and discussion

2.1. Volatilization and interaction in PbI_2 precursor solution

In this research, a two-step sequential deposition process was employed to create the formamidinium-based (FA-based) perovskite film. The initial step involved the deposition of a PbI_2 layer by spin-coating a PbI_2 precursor solution (comprising a solvent mixture of dimethylformamide (DMF) and dimethyl sulfoxide (DMSO) in a volume ratio of 9 : 1) onto the ITO/SnO_2 substrate. This layer was then annealed at 70 °C for 1 min in a N_2 atmosphere, constituting the first thermal-annealing step. Subsequently, an organic ammonium salt solution (containing formamidinium iodide (FAI), methylammonium iodide (MAI), and methylammonium chloride (MACl) in isopropyl alcohol) was spin-coated onto the PbI_2 layer. This was followed by a 15-minute aging process at 150 °C under ambient atmospheric conditions (30–40% humidity), serving as the second thermal-annealing step. The solid additives were introduced into the PbI_2 precursor solution.[19,41]

Fig. 1a provides an illustration of the molecular structures and electrostatic potential mapping of CP and CQ, along with their respective net dipole moments. These values were determined through density functional theory calculations using the B3LYP/6-31G* basis set.[42] Notably, both CP and CQ exhibit strong negative electrostatic potential at the carbonyl (C═O) moiety. However, CQ possesses a larger net dipole moment (5.39 Debye) compared to CP (3.30 Debye), as shown in Table S1 (ESI†). This difference indicates that CQ, being a Lewis base, can effectively interact with uncoordinated Pb trap sites and FA^+ ions present on the perovskite surface when introduced into the perovskite film.[43,44]

As shown in Fig. 2a for typical thermogravimetric analysis (TGA), relative to CQ, CP is a more volatile solid molecule with a clear weight loss starting at ~40 °C. In the case of PbI_2 samples mixed with these additives (in a 1 : 1 (wt/wt)), similar trends are observed. Their differential scanning calorimetry (DSC) measurements identify that the volatilization of CP and CQ rather

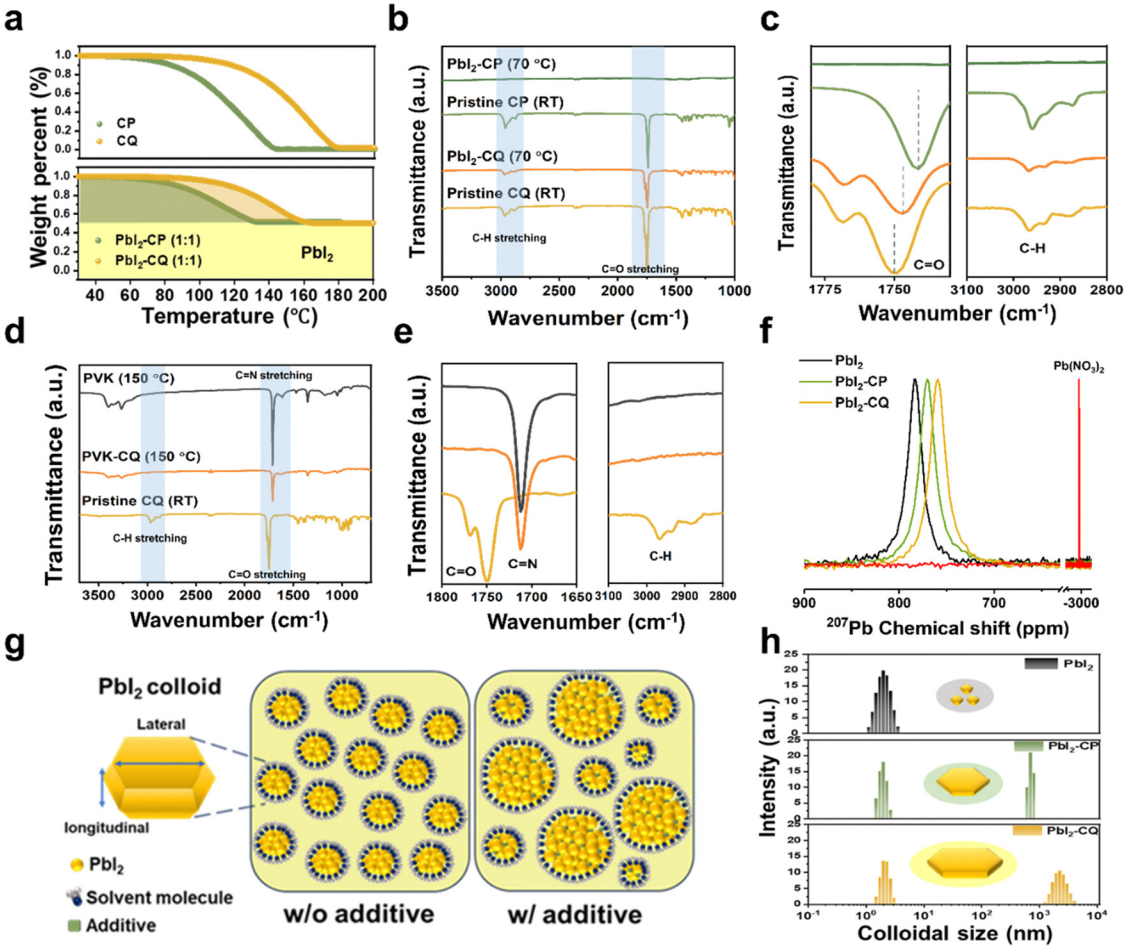

Fig. 2 Volatility and interaction of CP and CQ additives. (a) TGA plots of CP and CQ (pristine and blended with PbI_2). (b) The whole range and (c) magnified FTIR spectra of CP (RT), CQ (RT), PbI_2-CP (70 °C), and PbI_2-CQ (70 °C). (d) The whole range and (e) magnified FTIR spectra of CQ, PVK-CQ (150 °C), and PVK without CQ (150 °C). (f) ^{207}Pb NMR spectra of PbI_2, PbI_2-CP, and PbI_2-CQ, where the samples were calibrated by $Pb(NO_3)_2$, which represents −2959.7 ppm. (g) Schematic diagram of the PbI_2 colloids (with or without additive). (h) DLS measurements of pristine PbI_2, PbI_2-CP, and PbI_2-CQ. The inset shows the schematic diagram of the evolution of PbI_2 flakelets.

than their decomposition also occurs during the thermal-annealing process (see Fig. S1, ESI†). Fig. S2 (ESI†) presents their isothermal TGA curves over time at 70 °C as the first annealing step of PSC fabrication, showing that the mass loss rate of CP is far higher than that of CQ. Besides, it is also found that CP has higher vapor pressure (500.64 Pa) determined by the Langmuir equation in comparison to CQ (68.20 Pa) (see Table S2 and Note S1 for details, ESI†). From the above results, we can conclude that CP has very high volatilization kinetics during the first thermal-annealing step.

To further investigate the distinct volatilities of CP and CQ, Fourier transform infrared (FTIR) spectroscopy was utilized. Fig. 2b illustrates the stretching vibrations of the C═O groups for CP and CQ at 1741 and 1750 cm^{-1}, respectively. When both additives were heated at the same temperature of 70 °C, corresponding to the first thermal-annealing step, the C═O peak in the CP-mixed PbI_2 completely disappeared. Note that this volatilization of CP mainly occurred during the thermal annealing process rather than the spin-coating process (see Fig. S5, ESI†). In contrast, in the CQ-mixed PbI_2, the C═O peak still existed but shifted to a lower wavenumber of 1746 cm^{-1}. This indicates the efficient formation of coordinating bonds between the C═O group of CQ and Pb^{2+} through Lewis base–acid interactions, which reduces the electron density around the C═O bond, thereby weakening its strength and resulting in a shift to a lower wavenumber.[45,46] Additionally, it is noteworthy that the stretching vibrations of C–H peaks in 2950 cm^{-1} follow the same trend as that of the C═O group (Fig. 2c). Interestingly, during the second thermal-annealing step at 150 °C, the CQ solid additive completely volatilized, as evidenced by the absence of the C═O and C–H peaks (Fig. 2d and e). Note that the C═N peak of perovskite film at 1712 cm^{-1} should be distinguished from the C═O group of CQ.

To further confirm the complete evaporation of CP and CQ, ^1H-nuclear magnetic resonance (NMR) analysis was performed on the *ex situ* taken films at each processing step, as shown in Fig. S6–S8 (ESI†). The experimental details are described in Note S2 (ESI†). The *ex situ* ^1H-NMR study clearly demonstrates that CP and CQ are completely volatilized during the first and second thermal annealing processes, respectively.

Furthermore, the quantification of residual CP and CQ at each processing step was conducted using liquid chromatography-mass spectroscopy (LC-MS) (for details, see Fig. S9–S14 and Note S3, ESI†). As shown in Table S3 (ESI†), CP exhibits negligible residues, whereas most of CQ remains after the first annealing step. The remaining CQ is fully evaporated during the second annealing step. Collectively, these results identify CP as a volatile solid additive and CQ as a stepwise volatile solid additive, based on their distinct volatilization kinetics.

We conducted ^{207}Pb NMR analysis in a deuterated DMF : DMSO solution (9 : 1, v/v) as shown in Fig. 2f. It is important to note that we characterized the PbI_2 precursors and perovskites both without and with the optimal amounts of CP (30 mM) and CQ (3.0 mM) solid additives, respectively. These conditions were optimized for PSC fabrications, as detailed in the following photovoltaic section. The ^{207}Pb resonance signal for pristine PbI_2 was at 782.8 ppm, but it clearly shifted to a lower frequency in the additives-mixed PbI_2 adducts. This shift was a result of the different Pb coordination environments induced by Lewis base–acid interactions.[47] Note that the CQ-mixed PbI_2 exhibited a more pronounced up-field shift, indicating a stronger Pb–CQ coordination environment.

Moreover, we performed ^{13}C-NMR spectroscopy measurements to further the additive-PbI_2 coordination interaction. Fig. S15 and S16 (ESI†) display the ^{13}C-NMR resonance signals of the carbons in the C═O bonds of CP and CQ molecules, respectively. In additive-mixed PbI_2 solutions, the peaks clearly down-shifted with increasing additive concentrations. These results are due to the different chemical environments of the C═O bond within the additive molecules after the Lewis base–acid interaction with the electron-deficient Pb^{2+} moiety. These observations align with the result of ^{207}Pb NMR measurement showing the up-shifted resonance signals of the additive-Pb^{2+} adducts. Furthermore, in the results of diffusion ordered spectroscopy (DOSY) NMR measurements (Fig. S17–S20, ESI†), the diffusion coefficient (D) of CP and CQ decreased with increasing concentration of Pb^{2+} sites, where the D is related to the hydrodynamic radius of the nanostructure size in the PbI_2-additive mixture (see Table S4 for details, ESI†). These results indicate the increased nanocrystal sizes of additive-mixed PbI_2 colloidals, which are a result of the enhanced interaction between additives and Pb^{2+} sites. Collectively, we conclude that there are strong coordinative interactions between the C═O bonds of the CP and CQ molecules and the Pb^{2+} site of the PbI_2.

To assess the impact of CP and CQ on the size of PbI_2 colloids, we conducted dynamic light scattering (DLS) measurements of the PbI_2 precursor solutions (DMF : DMSO). Fig. 2g illustrates that the pristine PbI_2 colloids consist of (001) and (101) facets. It is known that layered PbI_2 structures can be exfoliated by solvent molecules through the (101) facet or vacancies on the (001) facet due to strong coordination between polar solvent molecules and Pb^{2+}.[48–55] Fig. 2h presents histograms of the colloidal size distributions, showing that PbI_2-pristine colloids exhibit flakelets along the (001) plane with a longitudinal dimension of ~1 nm and no detectable lateral dimension. In contrast, the CP- and CQ-mixed PbI_2 colloids display flakelets with similar longitudinal dimensions but significantly larger lateral dimensions of 726.7 nm and 2392.2 nm, respectively. We attribute the laterally enlarged PbI_2 plates to additional coordination interactions between the C═O group of the additives and Pb^{2+}, which may hinder the intercalation of solvent molecules into the PbI_2 (101) facets. The noticeable shift of the additive-mixed PbI_2 in the ultraviolet-visible (UV-vis) spectra to a longer wavelength validates the interpretation from DLS data (Fig. S14, ESI†).[56] In particular, the significant redshift in the CQ-mixed PbI_2 can be partially attributed to the chromophore in the CQ molecule, which shows absorption in the 400 to 500 nm range in the pristine CQ (Fig. S21, ESI†).

2.2. Morphological characterization of the PbI_2 layer

The surface morphologies of the PbI_2 precursor films after the first thermal-annealing step were examined using scanning electron microscopy (SEM). As depicted in Fig. 3a, the PbI_2-pristine film exhibits a compact texture with small grains. In contrast, the CP- and CQ-treated PbI_2 films exhibited enlarged grain sizes with a greater number of pinholes (mean cluster sizes of 99.9 nm, 161.2 nm, and 180.5 nm for PbI_2-pristine, CP-treated, and CQ-treated PbI_2 films, respectively; Fig. 3b). This observation aligns with the changes in absorption and intensity shifts observed in their UV-vis spectra. Specifically, the CP- and CQ-treated PbI_2 films exhibit higher absorptivity with red-shifting compared to the PbI_2-pristine film (Fig. S22, ESI†). Additional evidence of relatively larger grains and more pinholes in CQ-treated PbI_2 films is provided by their atomic force microscopy (AFM) images (Fig. 3a). The increased cluster sizes and porosities in the CP- and CQ-treated PbI_2 films facilitate the formation of a mesoporous structure, enhancing the penetration of FAI into the PbI_2 framework. This results in a high-quality perovskite film with fewer nucleation sites and larger perovskite grain sizes.[26,50,57,58] To investigate the impact of CP and CQ solid additives on the crystallinity of PbI_2 films, we conducted grazing incident wide angle X-ray scattering (GIWAXS). In this analysis, the incident angles were set to 0.13° and 1.0° to gather information on the near-surface region and the full depth of the films, respectively (Fig. 3c–e and Fig. S23, ESI†). At an incident angle of 0.13°, the PbI_2-pristine film exhibits the PbI_2 (001) peak at approximately q = 0.9 Å^{-1}, consistent with previous reports.[59–61] However, when treated with the solid additives, we observe not only additional shoulder peaks at q = ~0.87 Å^{-1} and ~0.96 Å^{-1} but also a shift in the position of the (001) peak. These results correlate with the broadening of cluster size distributions in CP- and CQ-mixed PbI_2 (see Table S5 for a comparison of the standard deviation values, ESI†). Specifically, the (001) peak shifts to higher q vectors for CP-treated PbI_2 and to lower q vectors for CQ-treated PbI_2 films (Fig. S24 and S25, ESI†). These observations suggest that the CP and CQ treatments induce changes in the lattice d-spacing of the PbI_2 surfaces. At a higher incident angle (1.0°), all the films exhibit no visible shoulder peaks, and the PbI_2 (001) peak is almost identical but shifted to lower q

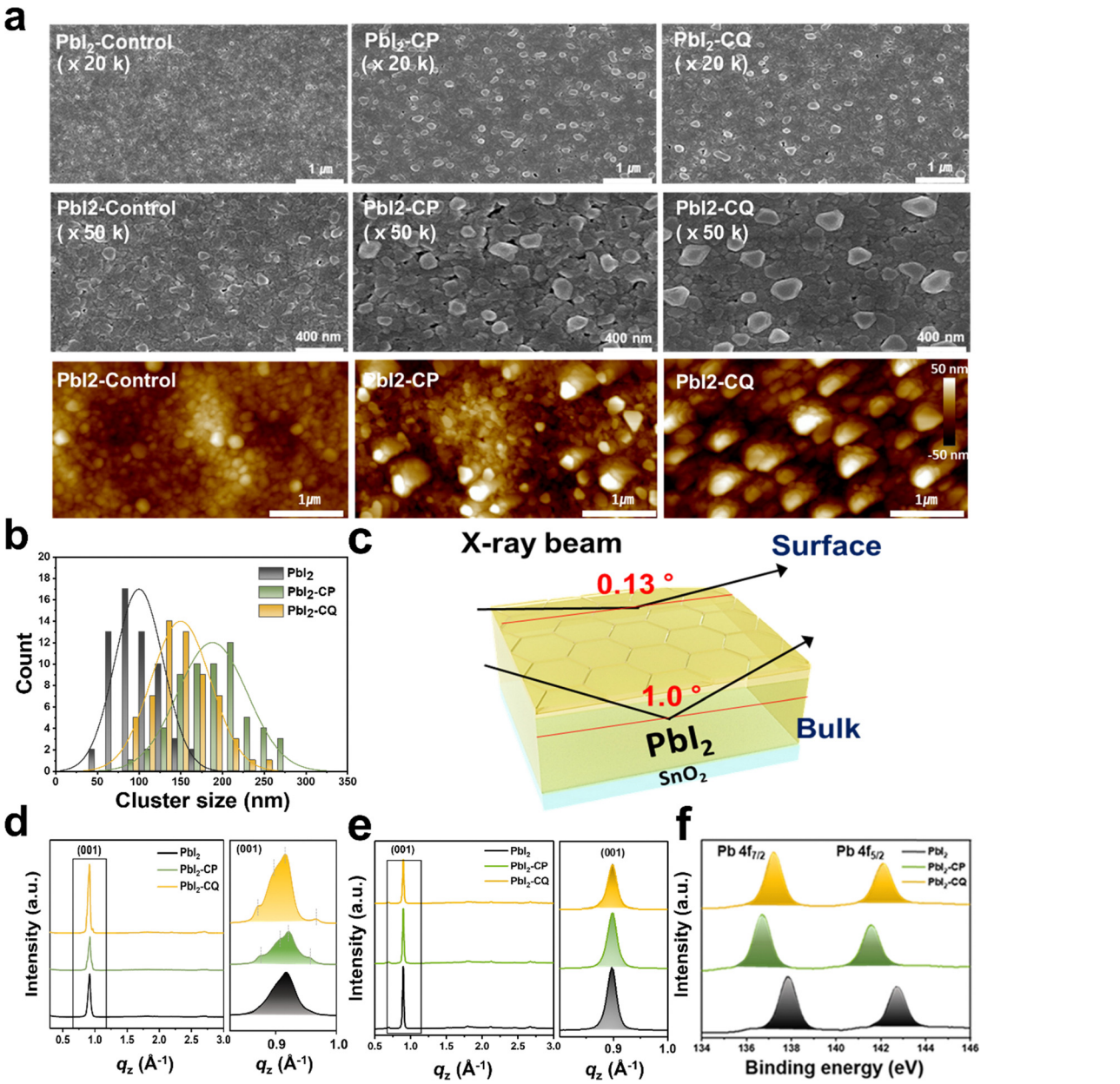

Fig. 3 Effect of CP and CQ additives on PbI_2 film morphology. (a) Top-view SEM images of PbI_2-control, CP, and CQ with AFM images of the inset (4 μm × 4 μm). (b) Cluster size distribution of pristine PbI_2, PbI_2-CP, and PbI_2-CQ. (c) Schematic illustration of the angle-dependent 2D-GIWAXS measurement. Line-cut profile of PbI_2 (001) of the control, CP-, and CQ-PbI_2 for (d) 0.13 and (e) 1.0° incident angles. (f) XPS spectra (Pb 4f) of PbI_2 pristine, PbI_2-CP, and PbI_2-CQ.

vectors relative to what is observed at the low incident angle. Transmission electron microscopy (TEM) measurement was also applied to further elucidate the influence of the CP and CQ treatment on PbI_2 lattice surfaces (Fig. S26, ESI†). The pristine PbI_2 shows the lattice distance of 3.64 Å, which can match with the (110) plane of the hexagonal PbI_2 phase. Note that the PbI_2 (001) lattice does not appear since the ultrasonicated PbI_2 powder dispersion method is involved to prepare appropriate TEM samples. Interestingly, the lattice distances of the CP- and CQ-treated PbI_2 are changed to 3.46 Å and 3.97 Å, respectively. These results show good agreement with the opposite trend in the lattice *d*-spacing seen from the GIWAXS above.

We conducted X-ray photoelectron spectroscopy (XPS) of the films to characterize the core-level binding energies (BEs) of the PbI_2 film surfaces (Fig. 3f and Fig. S27, ESI†). The XPS pattern of Pb 4f for the PbI_2-pristine film displays two dominant peaks at 137.88 and 142.68 eV, corresponding to the Pb $4f^{7/2}$ and Pb $4f^{5/2}$, respectively. Both peaks are shifted toward lower BEs for both CP- and CQ-treated PbI_2 films, indicating an enriched electron environment of Pb in the additives-containing PbI_2 lattices.[62] A closer examination of the XPS data reveals a slightly larger shift for the CP-treated case, suggesting the formation of denser PbI_2 film surfaces through the complete volatilization of CP after the first thermal-annealing step. Collectively, the data

presented highlight the distinct roles played by CP and CQ solid additives during the processing of PbI_2 films.

To elaborate, during the first thermal-annealing step: (i) CP entirely evaporates, resulting in the filling of voids with PbI_2 and the consequent formation of a denser PbI_2 film, particularly on the surfaces. (ii) In contrast, the complete volatilization of CQ molecules is constrained by their inherent Lewis base–acid interaction, as described above. Certain CQ molecules undergo partial volatilization, acting as a mediator for PbI_2 surface packing similar to CP. However, a number of them remain within the PbI_2 bulk film, serving as passivating agents for PbI_2 defects owing to their inherently enhanced Lewis base–acid interaction, as discussed earlier. A schematic representation of the microstructure evolution during PbI_2 film formation with CP and CQ is provided in Fig. S28 (ESI†).

2.3. Morphological characterizations of the perovskite film

To fabricate FA-based perovskite films, we initiated the reaction with FAI, followed by the second thermal-annealing process at 150 °C, as previously described. We conducted top-view and cross-sectional SEM analyses to assess the influence of CP and CQ on perovskite grain growth. As illustrated in Fig. 4a, the grain sizes were approximately ~858 nm and ~1183 nm in the CP- and CQ-treated perovskite films, respectively. This increase in grain size can be attributed to the reduced nucleation density resulting from the enlarged PbI_2 cluster sizes. These grain sizes are significantly larger than those of the control perovskite film without any additives, which had an average grain size of approximately ~608 nm (Fig. 4b and Table S6, ESI†). Relative to the control perovskite film, both CP- and CQ-treated perovskite films exhibit higher absorbance, partially reflecting the improved crystallinity driven by the larger grain sizes (Fig. S29, ESI†).

To further investigate the crystal quality and orientation of the perovskite films, we analyzed depth GIWAXS at different incident angles (0.13° and 1.0°) and examined their polar intensity profiles of the integrated semicircle (110) peak at azimuthal angles ranging from 0° to 180° (Fig. S30, ESI†). The CP- and CQ-treated perovskite films exhibit increased intensities of the perovskite peaks compared to the control perovskite film. In Fig. 4c and d, intensity-corrected pole figures reveal two peaks at azimuthal angles near 35° & 145° and 90°, which

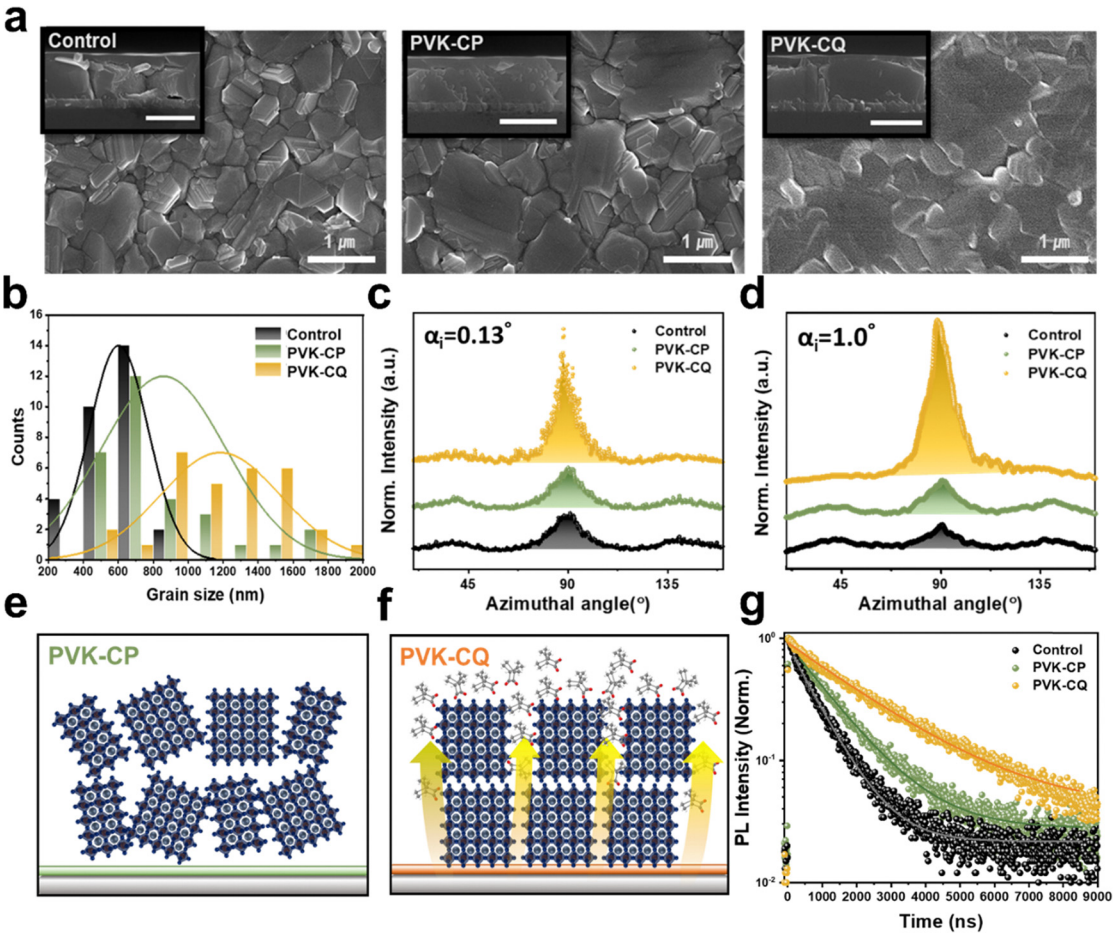

Fig. 4 Characterization of perovskite films. (a) Top-views and cross-sectional SEM images of the control, CP-, and CQ-treated perovskites (PVKs). (b) Grain size distribution of the control, CP-, and CQ-based PVKs. Polar intensity plots azimuthally along the ring at q = 1.00 $Å^{-1}$ of the control, CP-, and CQ-PVKs for (c) 0.13° and (d) 1.0° incident angles. Schematic illustration for the proposed (110) facet stacking mode in (e) CP- and (f) CQ-treated PVK films. (g) TRPL plots of the control, CP-, and CQ-treated PVKs.

correspond to the orientations of perovskite crystal stacking relative to the substrate. Across all the films, the intensity of the latter peak is higher than that of the former, regardless of the incident angles, indicating a greater prevalence of perovskite crystal stackings oriented perpendicular to the film plane. At a low incident angle (0.13°), the area ratios of the two peaks (the latter-to-the former) follow the sequence of the control (1.74) ≅ CP (1.84) < CQ (4.01)-treated perovskite films, suggesting a higher degree of preferred orientation in the CQ-treated perovskite film (Table S7, ESI†). This difference in preferred crystallographic orientations becomes more pronounced in the bulk films, as evidenced by the ratio values of the two peaks at a high incident angle (1.0°). These results demonstrate that CQ can effectively manipulate the crystallographic orientation, and the proposed stacking modes are schematically depicted in Fig. 4e and f. Time-resolved photoluminescence (TRPL) was further measured to estimate the carrier lifetimes of the control, CP-, and CQ-modified perovskite films using a picosecond laser with a wavelength of 450 nm (Fig. 4g). All three samples display mono-exponential decay related to trap-assisted recombination. The corresponding carrier lifetimes, obtained from TRPL fitting line, were 788 ns, 1126 ns, and 2130 ns for the control, CP-, and CQ-treated devices, respectively. These results indicated that the CQ additive improved the crystallinity and preferred orientation of the perovskite, prolonging charge carrier lifetime and reducing trap-assisted recombination.

We further investigated the effect of additive concentration on the morphological changes of PbI_2 and perovskite films through SEM measurement (Fig. S31, ESI†). As the concentration of CP increases, both the number of PbI_2 clusters and the perovskite grain size grow, achieving an optimal morphology at 30 mM. However, at a higher concentration (60 mM), excessively large and dense PbI_2 clusters were formed, which are difficult to convert to a high-quality perovskite layer due to inhomogeneous and disturbed perovskite crystallization. This leads to the defects and non-uniform crystal growth of perovskite, ultimately degrading the device performance (see PSC data later). Similarly, in the case of CQ, concentrations up to 3 mM promoted enlarged and smoothed perovskite grains; however, at higher concentration of 6 mM, excessive amounts of CQ induced microporous surface structures in the perovskite layer. These voids significantly contributed to severe degradation in both device performance and operational stability. As shown in Fig. S32 (ESI†), the use of even higher CQ concentration (30 mM) leads to an increase in pores from the bottom to the top, which significantly reduced the operational stability (Fig. S33, ESI†).

2.4. *In situ* PL measurements of perovskite film formation

To gain a deep insight into the kinetics of volatile additives in FA-based perovskite crystallization, *in situ* PL measurements were performed during second thermal annealing at 150 °C using an excitation wavelength of 520 nm (Fig. 5a). After the FAI solution was spin-coated onto PbI_2 films, the dark brown film was immediately transferred to a hot plate under controlled humidity (relative humidity of 40%). The FA-based perovskite

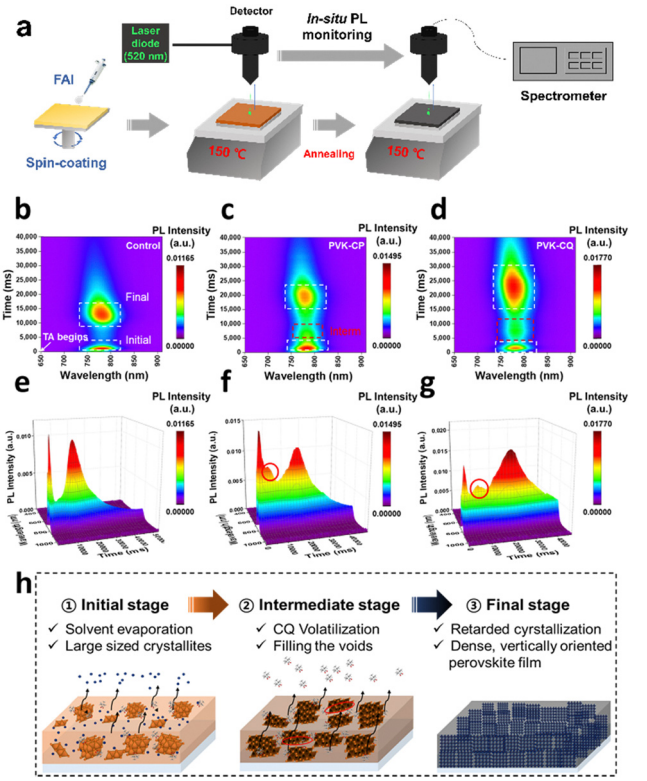

Fig. 5 *In situ* PL measurements during the FA-based PVK crystallization. (a) Schematic illustration of *in situ* PL monitoring during the FA-based PVK crystallization (150 °C). Heatmaps of *in situ* PL of the FA-based PVK film for (b) control, (c) PVK-CP, and (d) PVK-CQ. 3D colormap surfaces of *in situ* PL of the FA-based PVK film for (e) control, (f) PVK-CP, and (g) PVK-CQ. (h) Schematic summary showing the effects of CQ in crystallization kinetics.

crystallization starting with the annealing process was simultaneously monitored as a function of time in the PL response. Fig. 5b displayed the heat maps of the PL intensity for the control, CP-, and CQ-treated perovskite films (the detailed spectra are shown in Fig. S34, ESI†). All three samples exhibited instantaneous PL peaks in the initial stage of FA-based perovskite film formation (from 0 to 2500 ms). The initial evaporation of the remaining solvent in the precursor film leads to supersaturation of the solute and plenteous nuclei are formed at this stage.[63–65] In the final stage, the PL spectra of the control perovskite film reached its maximum intensity of 1.081×10^4 for 13 200 ms. Note that the PL intensity started to decrease after reaching the peak due to thermal quenching caused by continuous heating.[66–68] Compared to the control perovskite film, both CP- and CQ-treated perovskite films exhibit an intermediate stage in the PL spectra between the initial stage and final stage (Fig. 5c). We speculate that this preliminary phase transition is attributed to the larger sized crystallites due to the CP and CQ additives, as confirmed by previous DLS measurements. These intermediate states are more pronounced in the CQ-based perovskite film (from 5000 to 10 000 ms). In the final stage, the CQ-treated perovskite film shows the most delayed film formation time of 22 890 ms with the highest maximum intensity of 1.770×10^4, indicating that the volatile CQ serves to

retard the crystallization of the FA-based perovskite for the highly crystalline perovskite.[62,69] As illustrated in Fig. 5d, upon transition from the intermediate to the final state, the volatile CQ molecules completely evaporate, filling the voids with perovskite, and finally resulting in the formation of a dense and vertically oriented perovskite film.

Additionally, the evolutions of film colors during the total process (from the initial PbI_2 film to the final PVK film) were monitored over time to additionally exhibit the retardation of the CQ-assisted crystallization process (Fig. S35, ESI†). Compared to the initial control PbI_2 film, the CQ-PbI_2 film exhibited a more pronounced yellow and transition to a more orange color upon treatment with FAI solution. This more orange film was attributed to the much disordered PbI_6 octahedra connectivity, which was a result of the interaction between CQ molecules and Pb^{2+} ions. During 5 min of FAI penetration, the CQ intermediate film darkened to a brown and transformed into a distinct black FA-based perovskite film after the second-stage annealing. This progression indicated that CQ treatment effectively retarded the crystallization process, resulting in a more compact and highly oriented perovskite structure.

2.5. Photovoltaic performances

We constructed planar n–i–p PSCs with the structure ITO or FTO/SnO_2/$FA_{0.92}MA_{0.08}PbI_3$ perovskite layer/OAI (2D treatment)/spiro-OMeTAD/Au (refer to Fig. 6a for the schematic). These PSCs were fabricated both with and without the inclusion of solid additives to investigate their impact on device performance. After screening PSC results at various additive concentrations (ranging from 15 to 60 mM), the optimal concentrations were determined to be 30 mM for CP and 3 mM for CQ, respectively (Fig. S36 and S37, ESI†). Detailed device fabrication procedures are outlined in the Experimental section. Note that even trace amounts of the solid additives in the PSCs, at different concentrations, induced significant variations in device performance, underscoring their pronounced influence on PSC characteristics. Fig. 6b illustrates the current density–voltage (J–V) curves for the optimized control, CP-treated, and CQ-treated PSCs (active area = 0.042 cm^{-2}, under AM 1.5G 1-sun illumination), and the pertinent photovoltaic parameters are summarized in Table 1. For the optimized control device with a $FA_{0.92}MA_{0.08}PbI_3$ perovskite, a PCE of 22.60% was achieved, with

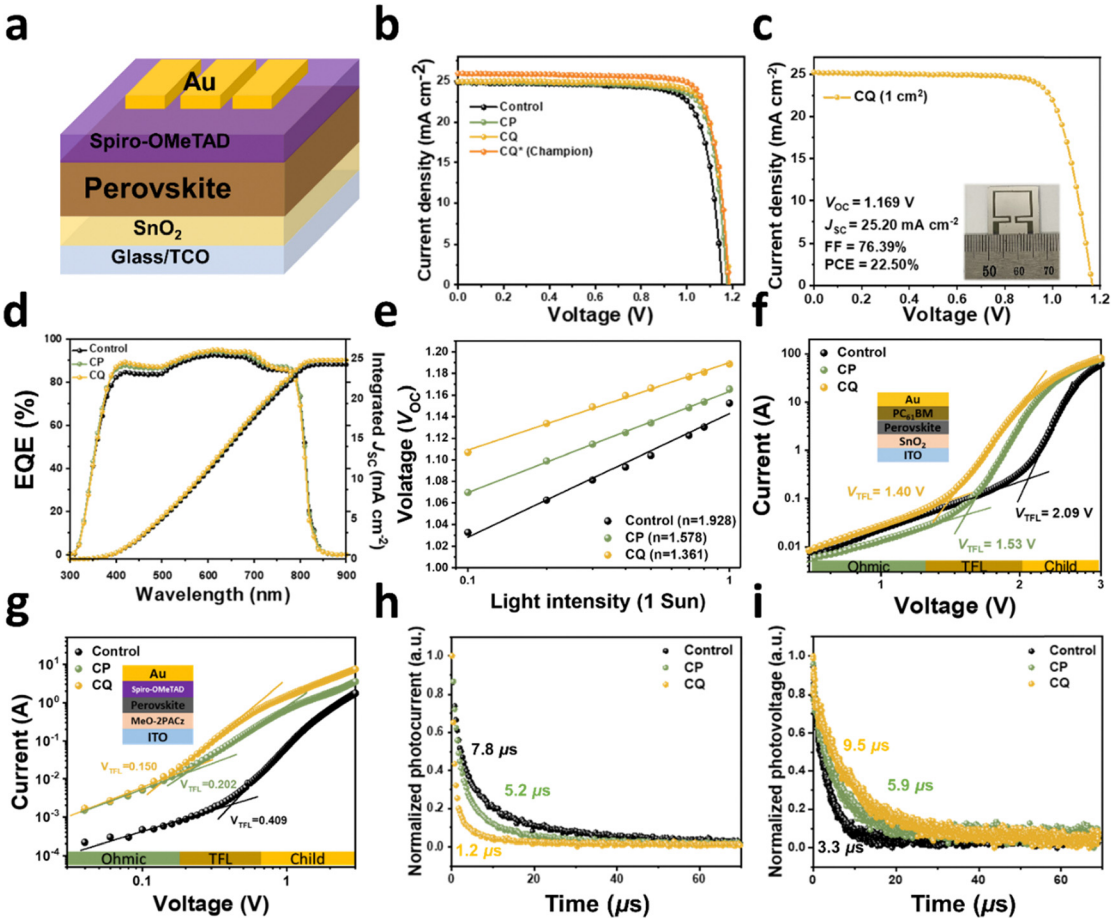

Fig. 6 Photovoltaic performance. (a) N–i–p device architecture. (b) J–V curves of the control, CP- and CQ-treated devices (reverse scan). The champion device was fabricated with architecture of the FTO/chemical bath deposited SnO_2 with the anti-reflecting film for enhanced current density. (c) J–V curve of the CQ-treated large-area device (area: 1 cm^{-2}). (d) EQE spectra and integrated J_{SC} plots. (e) The semi-logarithmic plots of light intensity *versus* V_{OC}. SCLC measurements for the (f) electron-only devices (ITO/SnO_2/perovskite/$PC_{61}BM$/Au) and (g) hole-only devices (ITO/MeO-2PACz/perovskite/spiro-OMeTAD/Au). (h) TPC and (i) TPV measurements of the control, CP-, and CQ-based devices.

Table 1 Photovoltaic performances of PSCs with different solid additives (reverse scan)

Device	V_{OC} [V]	J_{SC} [mA cm^{-2}]	J_{SC}^{cal} [mA cm^{-2}]	FF [%]	PCE [%]
Control	1.153 (1.148 ± 0.017)[b]	24.86 (24.49 ± 0.76)[b]	24.32[a]	78.81 (77.64 ± 2.46)[b]	22.60 (21.84 ± 0.65)[b]
CP	1.173 (1.163 ± 0.009)[b]	24.96 (24.90 ± 0.56)[b]	24.85[a]	80.69 (80.00 ± 1.34)[b]	23.63 (23.17 ± 0.48)[b]
CQ	1.187 (1.170 ± 0.007)[b]	24.99 (24.97 ± 0.35)[b]	24.86[a]	81.57 (80.29 ± 0.90)[b]	24.19 (23.47 ± 0.57)[b]
Control[c] (Champion)	1.156	25.12	25.16	79.93	23.20
CQ[c] (Champion)	1.183	25.95	25.81	81.45	25.00
CQ[c] (Certified)	1.186	25.75	—	81.48	24.89

[a] Calculated J_{SC} by EQE measurements. [b] The average values and standard deviations obtained from 24 devices. [c] The champion device was fabricated with the architecture of FTO/chemical bath deposited SnO_2/$Cs_{0.05}FA_{0.95}PbI_3$/OAI/spiro-OMeTAD/Au (an anti-reflecting film was used to enhance the current density).

an open-circuit voltage (V_{OC}) of 1.153 V, a short-circuit current (J_{SC}) of 24.86 mA cm^{-2}, and a fill-factor (FF) of 78.81%. Notably, significant performance enhancements were observed in the devices treated with optimal CP and CQ concentrations. In particular, the CQ-treated device achieved the enhanced PCE of 24.19%, accompanied by considerably increased V_{OC} (1.187 V) and FF (81.57%) values, surpassing those of both the control and CP-treated devices. Importantly, all the devices exhibited negligible hysteresis (Fig. S38 and Table S8, ESI†), and the J_{SC} values obtained from *J–V* scanning closely matched the values obtained by integrating the EQE spectra (24.32, 24.85, and 24.86 mA cm^{-2} for the control, CP-treated, and CQ-treated devices, respectively, Fig. 6d). For the control and CQ-based device, the stabilized power output and current density agree with those obtained from *J–V* measurements (Fig. S39 and S40, ESI†). To further validate these findings, Fig. S41 (ESI†) displays histograms of 24 individual devices for each case, confirming a narrower distribution of PSCs treated with additives compared to the control devices. We further optimized device fabrication to upgrade the champion device achieving higher PCE. The CQ-treated champion device achieved remarkable PCE of 25.00% with a V_{OC} of 1.183 V, J_{SC} of 25.95 mA cm^{-2}, and FF of 81.45% (Fig. S42 and Table S9, ESI†), where the J_{SC} value was well matched with the values obtained by integrating the EQE spectra (25.81 mA cm^{-2}) (Fig. S43, ESI†). One of the best CQ-treated devices obtained a certified PCE of 24.89% from an independent institute, which is comparable to those obtained from the two-step-based state-of-the-art devices (Fig. S44 and Table S10, ESI†). Additionally, the CQ-treated large-area devices (active area: 1.0 cm^2) were also fabricated to evaluate its scalability. As shown in Fig. 6c, the best-performing large-area device shows a high PCE of 22.50% with a V_{OC} of 1.169 V, J_{SC} of 25.20 mA cm^{-2}, and FF or 76.39%. This indicates improvement in charge-carrier dynamics, including reduced charge recombination and enhanced charge transport properties in the CQ-treated device, which shows a similar trend to reported studies on the preferentially oriented perovskite-based solar cells (Table S11, ESI†). To exhibit universality of stepwise volatilization of the CQ additive in two-step-based fabrication methodology, we applied the CQ additive to the Cs-containing A-cation system ($Cs_{0.05}FA_{0.95}PbI_3$) and mixed-halide perovskite system ($Cs_{0.05}FA_{0.95}Pb(I_{0.95}Br_{0.05})_3$).[70,71] The corresponding *J–V* characteristics and photovoltaic parameters are summarized in Fig. S45 and Table S12 (ESI†), respectively. In common with all systems, the CQ additive effectively enhanced V_{OC} and FF values. In particular, the CQ-treated $Cs_{0.05}FA_{0.95}PbI_3$ system showed better performance than that of the $FA_{0.92}MA_{0.08}PbI_3$-based previous system, which was attributed to the additional lattice stabilization through Cs-inclusion.

We also investigated the dependence of V_{OC} and J_{SC} on light intensity (P_{Light}) to gain further insights into the recombination mechanisms within the devices, as depicted in Fig. 6e. The semi-logarithmic plot of P_{Light} *versus* V_{OC} can be analyzed using $V_{OC} \propto (nk_BT)/q \ln(P_{Light})$, where n, k_B, T, and q represent the ideality factor, Boltzmann constant, temperature in Kelvin, and elementary charge, respectively. A lower slope approaching k_BT/q indicates a reduced contribution from trap-assisted recombination.[72,73] The calculated n values were found to be 1.69, 1.50, and 1.34 for the control, CP-, and CQ-treated devices, respectively. Additionally, the power-law equation $J_{SC} \propto P_{Light}^{\alpha}$ describes the P_{Light} *versus* J_{SC} relationship, where α denotes the extent of bimolecular recombination.[74] The control device exhibits an α value of 0.989, whereas the CP- and CQ-treated devices have α values of 0.992 and 0.993, as evident from Fig. S46 (ESI†). Combined together, these results indicate that both trap-assisted and bimolecular recombinations are effectively mitigated by the presence of solid additives, especially in the case of CQ.

Furthermore, we conducted an assessment of how the incorporation of solid additives affects trap-state density (N_t) within the perovskite films. Dark *J–V* characteristics were collected for electron-only devices with the structure of ITO/SnO_2/perovskite/[6,6]-phenyl-C_{61}-butyric acid methyl ester ($PC_{61}BM$)/Au and hole-only devices with the structure of ITO/MeO-2PACz/perovskite/spiro-OMeTAD/Au. As depicted in Fig. 6f and g, the dark *J–V* curves for all the perovskite devices exhibit a linear Ohmic response at low bias, followed by a trap-filled limit regime and a trap-free space-charge limited current (SCLC) regime. N_t and the trap-filled limit voltage (V_{TFL}) were determined using the equation $N_t = (2\varepsilon\varepsilon_0 V_{TFL})/(qL^2)$, where ε and ε_0 represent the relative dielectric constant of the perovskite (ε = 28.8) and the vacuum permittivity, respectively, and L denotes the thickness of the perovskite film (~730 nm).[75] For electron-only devices, the V_{TFL} values for the control, CP-, and CQ-treated devices were 2.09, 1.53, and 1.40 V, corresponding to N_t values of 1.25 × 10^{16} cm^{-3}, 0.92 × 10^{16} cm^{-3}, and 0.84 × 10^{16} cm^{-3}, respectively (Table S13, ESI†). In case of hole-only devices, the V_{TFL} values for the control, CP-, and CQ-based devices were 0.41, 0.20, and 0.15 V, resulting in N_t values of 2.45 × 10^{15} cm^{-3}, 1.20 × 10^{15} cm^{-3}, and 0.90 × 10^{15} cm^{-3},

respectively (Table S14, ESI†). These results confirm a reduction in trap density induced by the solid additives, consistent with the recombination studies mentioned earlier.

Transient photocurrent/photovoltage (TPC/TPV) decay curves were analyzed to investigate the behavior of charge carriers within the devices. TPC and TPV measurements were conducted under short-circuit and open-circuit conditions, respectively.[76] Fig. 6h reveals that photocurrent decay times, extracted from TPC, were 7.8 μs, 5.2 μs, and 1.2 μs for the control, CP-, and CQ-treated devices, respectively. The photovoltage decay time extracted from TPV (Fig. 6i) was 3.3 μs for the control device, but increased to 5.9 μs and 9.5 μs after treatment with CP and CQ, respectively. These results confirm the reduced recombination and improved charge extraction, especially in the case of CQ.

2.6. Stability evaluation

Finally, we compared the storage and thermal stabilities of the control, CP-, and CQ-treated devices. The storage stability test was conducted at 25 °C under 10% relative humidity without encapsulation, with the devices periodically exposed to simulated light for *J–V* testing. As depicted in Fig. 7a, the CP- and CQ-treated devices exhibited over 91.5% and 96.7% retention of their initial PCE values during 1608 hours, while the control device retained only 86.8%. Notably, the degradation in performance is primarily attributed to decreased FF, reflecting the decomposition of the perovskite crystals. We assessed the thermal stability of the devices at 85 °C in a nitrogen atmosphere. To exclude the influence of thermally unstable spiro-OMeTAD, the hole-transporting layer was replaced with PBDB-T-2F. Compared to a significant PCE degradation of 73.2% observed in the control device after continuous thermal stress for over 256 hours, the CP- and CQ-treated devices demonstrated excellent PCE retentions of 88.2% and 92.8% for over 312 hours, respectively, as depicted in Fig. 7b. Furthermore, we evaluated the operational stability of the encapsulated control and CQ-treated devices by maximum power point tracking (MPPT) under 1 sun illumination under ambient conditions (ISOS-L-1 protocol: temperature of 25 °C, ambient condition, Fig. 7c). The CQ-treated device maintained 90.1% of its initial PCE after 1000 h of MPPT, whereas the control device degraded to 80.8% of its original PCE after 500 h (Fig. S47 and Table S15, ESI†).

Additionally, the stability under combined heat and humidity stress was evaluated using the more rigorous ISOS-L-3 protocol, which involves MPPT at a temperature of 65 °C and a relative humidity of 50%. As shown in Fig. 5d, the CQ-treated device exhibits enhanced endurance against heat and humidity, maintaining 91.8% of its original PCE after 250 h, on the other hand, the control device degraded to 81.3% after 250 h. These improved stabilities can be attributed to the high-quality perovskite films with preferred orientation, as demonstrated previously, which provide a robust barrier against heat and light soaking conditions.

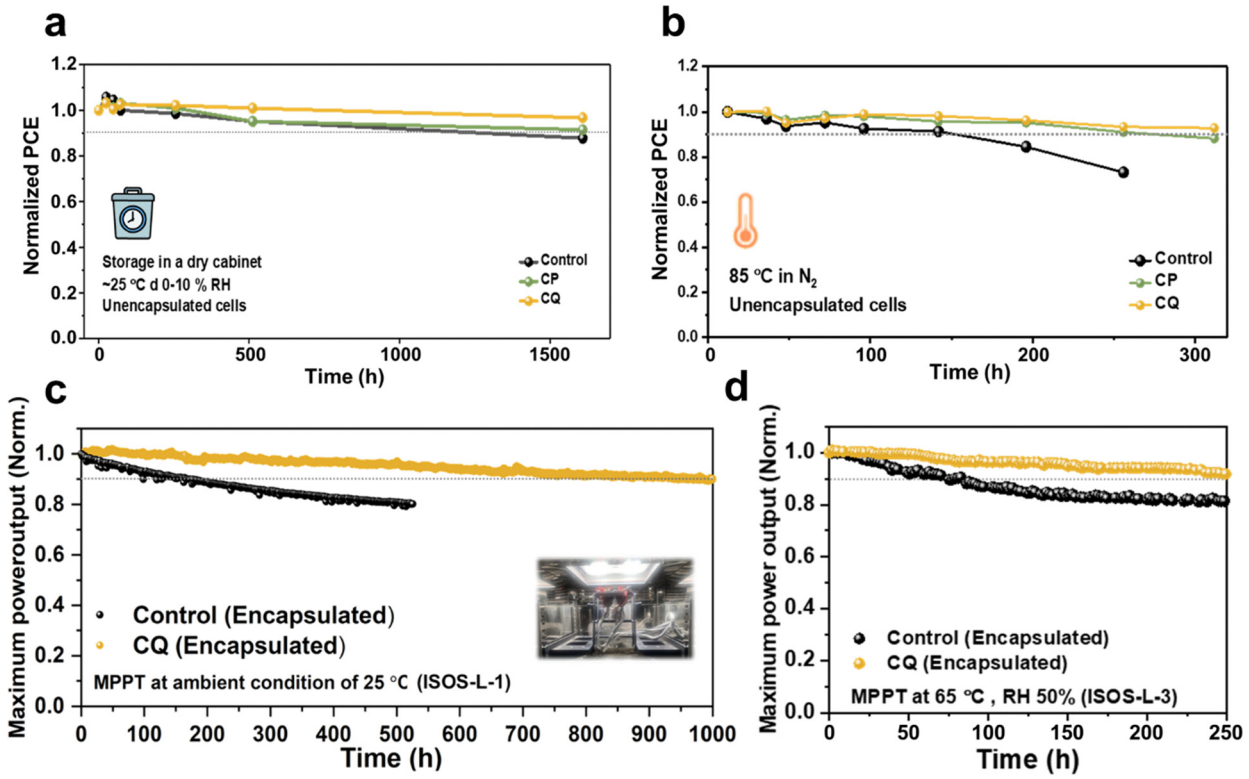

Fig. 7 Stability evaluation. (a) Storage stability of the control, CP-, and CQ-treated PSCs stored in a dry cabinet (~25 °C, RH of ~10%). (b) Thermal stability test of the control, CP-, and CQ-treated PSCs (~85 °C, N_2-filled glovebox). MPPT testing for the control and CQ-treated PSCs using (c) ISOS-L-1 and (d) ISOS-L-3, which was measured under full solar illumination (AM 1.5 G, 100 mW cm^{-2}) without a UV filter.

3. Conclusions

In summary, we introduced nature-sourced volatile solid additives, namely, CP and CQ, into PSCs to enhance their photovoltaic performance and stability. Through a comprehensive analysis using various characterization techniques, we observed distinct behaviors in the presence of these additives during the fabrication of PSCs *via* a two-stage thermal-annealing process. CP demonstrated complete volatilization during the first thermal-annealing step, resulting in the formation of a denser PbI_2 film. In contrast, CQ exhibited a stepwise-volatilization mechanism due to its stronger Lewis base–acid interaction with perovskite, facilitated by its bidentate coordination capability. This unique behavior resulted in high-quality FA-based perovskite crystallinity characterized by large-grained perovskite structures and a highly preferred crystallite orientation. As a result, the treatment with these solid additives significantly improved the efficiency and stability of PSCs compared to the control devices, with CQ treatment being particularly notable. It achieved an impressive PCE of 25.00% with a certified PCE of 24.89% and demonstrated excellent PCE retentions of 90.1% after 1000 hours under MPPT conditions. This study reports a pioneering advancement in enhancing PSCs using nature-sourced solid additives, furthering the eco-friendly processability of PSCs. This approach shows promise for enhancing other perovskite-based optoelectronic devices as well.

Author contributions

J. P. and C. Y. conceived the ideas and organized the work. J. P. conducted device fabrication and characterization and analyzed data. J. P. performed the morphology characterizations and analyzed the data. S. K. measured GIWAXS measurement and ^{207}Pb NMR data. W. K. conducted TGA measurements. S. Z. performed AFM measurements. B. L. conducted zeta-sizer measurements. J. P. and C. Y. contributed to the preparation and revision of this manuscript.

Data availability

The data that support the findings of this study are available within the article and its ESI.†

Conflicts of interest

The authors declare no competing interests.

Acknowledgements

This work was supported by the National Research Foundation of Korea (NRF) grant funded by the Korea government (MSIP) (2021R1A2C3004202), and the Korea Institute of Energy Technology Evaluation and Planning (KETEP) grant funded by the Korea government (MOTIE) (20213091010010, Super Solar cells-development of double junction solar cells, breakthrough for the theoretical limit of silicon solar cell efficiency (>35%)).

References

1 H. Chen, A. Maxwell, C. Li, S. Teale, B. Chen, T. Zhu, E. Ugur, G. Harrison, L. Grater, J. Wang, Z. Wang, L. Zeng, S. M. Park, L. Chen, P. Serles, R. A. Awni, B. Subedi, X. Zheng, C. Xiao, N. J. Podraza, T. Filleter, C. Liu, Y. Yang, J. M. Luther, S. De Wolf, M. G. Kanatzidis, Y. Yan and E. H. Sargent, *Nature*, 2023, **613**, 676–681.
2 M. A. Green, A. Ho-Baillie and H. J. Snaith, *Nat. Photonics*, 2014, **8**, 506–514.
3 M. Jeong, I. W. Choi, E. M. Go, Y. Cho, M. Kim, B. Lee, S. Jeong, Y. Jo, H. W. Choi, J. Lee, J.-H. Bae, S. K. Kwak, D. S. Kim and C. Yang, *Science*, 2020, **369**, 1615–1620.
4 M. Jeong, I. W. Choi, K. Yim, S. Jeong, M. Kim, S. J. Choi, Y. Cho, J.-H. An, H.-B. Kim, Y. Jo, S.-H. Kang, J.-H. Bae, C.-W. Lee, D. S. Kim and C. Yang, *Nat. Photonics*, 2022, **16**, 119–125.
5 Q. Jiang, R. Tirawat, R. A. Kerner, E. A. Gaulding, Y. Xian, X. Wang, J. M. Newkirk, Y. Yan, J. J. Berry and K. Zhu, *Nature*, 2023, **623**, 313–318.
6 J. J. Yoo, G. Seo, M. R. Chua, T. G. Park, Y. Lu, F. Rotermund, Y.-K. Kim, C. S. Moon, N. J. Jeon, J.-P. Correa-Baena, V. Bulović, S. S. Shin, M. G. Bawendi and J. Seo, *Nature*, 2021, **590**, 587–593.
7 Y. Zhou, C. Fei, M. A. Uddin, L. Zhao, Z. Ni and J. Huang, *Nature*, 2023, **616**, 712–718.
8 H.-S. Kim, C.-R. Lee, J.-H. Im, K.-B. Lee, T. Moehl, A. Marchioro, S.-J. Moon, R. Humphry-Baker, J.-H. Yum, J. E. Moser, M. Grätzel and N.-G. Park, *Sci. Rep.*, 2012, **2**, 591.
9 J.-W. Lee, D.-J. Seol, A.-N. Cho and N.-G. Park, *Adv. Mater.*, 2014, **26**, 4991–4998.
10 C. Ma, M.-C. Kang, S.-H. Lee, S. J. Kwon, H.-W. Cha, C.-W. Yang and N.-G. Park, *Joule*, 2022, **6**, 2626–2643.
11 J. S. Manser, J. A. Christians and P. V. Kamat, *Chem. Rev.*, 2016, **116**, 12956–13008.
12 C. K. MØLler, *Nature*, 1957, **180**, 981–982.
13 C. K. MØLler, *Nature*, 1958, **182**, 1436.
14 S. Pang, H. Hu, J. Zhang, S. Lv, Y. Yu, F. Wei, T. Qin, H. Xu, Z. Liu and G. Cui, *Chem. Mater.*, 2014, **26**, 1485–1491.
15 Y. Bai, Z. Huang, X. Zhang, J. Lu, X. Niu, Z. He, C. Zhu, M. Xiao, Q. Song, X. Wei, C. Wang, Z. Cui, J. Dou, Y. Chen, F. Pei, H. Zai, W. Wang, T. Song, P. An, J. Zhang, J. Dong, Y. Li, J. Shi, H. Jin, P. Chen, Y. Sun, Y. Li, H. Chen, Z. Wei, H. Zhou and Q. Chen, *Science*, 2022, **378**, 747–754.
16 J. Jeong, M. Kim, J. Seo, H. Lu, P. Ahlawat, A. Mishra, Y. Yang, M. A. Hope, F. T. Eickemeyer, M. Kim, Y. J. Yoon, I. W. Choi, B. P. Darwich, S. J. Choi, Y. Jo, J. H. Lee, B. Walker, S. M. Zakeeruddin, L. Emsley, U. Rothlisberger, A. Hagfeldt, D. S. Kim, M. Grätzel and J. Y. Kim, *Nature*, 2021, **592**, 381–385.
17 J. Park, J. Kim, H.-S. Yun, M. J. Paik, E. Noh, H. J. Mun, M. G. Kim, T. J. Shin and S. I. Seok, *Nature*, 2023, **616**, 724–730.

18 P. Shi, Y. Ding, B. Ding, Q. Xing, T. Kodalle, C. M. Sutter-Fella, I. Yavuz, C. Yao, W. Fan, J. Xu, Y. Tian, D. Gu, K. Zhao, S. Tan, X. Zhang, L. Yao, P. J. Dyson, J. L. Slack, D. Yang, J. Xue, M. K. Nazeeruddin, Y. Yang and R. Wang, *Nature*, 2023, **620**, 323–327.
19 Y. Zhao, F. Ma, Z. Qu, S. Yu, T. Shen, H.-X. Deng, X. Chu, X. Peng, Y. Yuan, X. Zhang and J. You, *Science*, 2022, **377**, 531–534.
20 X. Cao, L. Zhi, Y. Li, F. Fang, X. Cui, Y. Yao, L. Ci, K. Ding and J. Wei, *J. Mater. Chem. C*, 2017, **5**, 7458–7464.
21 C. Liu, X. Xu, Z. Zhang, S. Cao, J. Han, Y. Zheng, Z. Bi, Y. Zhu, S. Luo, G. Xu, S. Liu, K. Wang, Z. Ren, G. Li, Q. Deng and J. Liu, *J. Solid State Chem.*, 2023, **326**, 124195.
22 K. Liu, S. Rafique, S. F. Musolino, Z. Cai, F. Liu, X. Li, Y. Yuan, Q. Bao, Y. Yang, J. Chu, X. Peng, C. Nie, W. Yuan, S. Zhang, J. Wang, Y. Pan, H. Zhang, X. Cai, Z. Shi, C. Li, H. Wang, L. Deng, T. Hu, Y. Wang, Y. Wang, S. Chen, L. Shi, P. Ayala, J. E. Wulff, A. Yu and Y. Zhan, *Joule*, 2023, **7**, 1033–1050.
23 R. Wang, A. Altujjar, N. Zibouche, X. Wang, B. F. Spencer, Z. Jia, A. G. Thomas, M. Z. Mokhtar, R. Cai, S. J. Haigh, J. M. Saunders, M. S. Islam and B. R. Saunders, *Energy Environ. Sci.*, 2023, **16**, 2646–2657.
24 G. Zeng, G. Liu and X. Li, *ACS Sustainable Chem. Eng.*, 2023, **11**, 7664–7672.
25 P. Zhang, N. Gu, L. Song, X. Chen, P. Du, L. Zha, W.-H. Chen and J. Xiong, *Nanoscale*, 2022, **14**, 5204–5213.
26 T. Zhou, Z. Xu, R. Wang, X. Dong, Q. Fu and Y. Liu, *Adv. Mater.*, 2022, **34**, 2200705.
27 B. Fan, W. Zhong, W. Gao, H. Fu, F. R. Lin, R. W. Y. Wong, M. Liu, C. Zhu, C. Wang, H.-L. Yip, F. Liu and A. K. Y. Jen, *Adv. Mater.*, 2023, **35**, 2302861.
28 D. Hu, H. Tang, S. Karuthedath, Q. Chen, S. Chen, J. I. Khan, H. Liu, Q. Yang, J. Gorenflot, C. E. Petoukhoff, T. Duan, X. Lu, F. Laquai and S. Lu, *Adv. Funct. Mater.*, 2023, **33**, 2211873.
29 J. Oh, S. Jung, S.-H. Kang, G. Park, M. Jeong, S. Kim, S. Lee, W. Kim, B. Lee, S. M. Lee and C. Yang, *J. Mater. Chem. A*, 2022, **10**, 20606–20615.
30 J. Qin, Q. Yang, J. Oh, S. Chen, G. O. Odunmbaku, N. A. N. Ouedraogo, C. Yang, K. Sun and S. Lu, *Adv. Sci.*, 2022, **9**, 2105347.
31 L. Ye, Y. Cai, C. Li, L. Zhu, J. Xu, K. Weng, K. Zhang, M. Huang, M. Zeng, T. Li, E. Zhou, S. Tan, X. Hao, Y. Yi, F. Liu, Z. Wang, X. Zhan and Y. Sun, *Energy Environ. Sci.*, 2020, **13**, 5117–5125.
32 R. Yu, H. Yao, L. Hong, Y. Qin, J. Zhu, Y. Cui, S. Li and J. Hou, *Nat. Commun.*, 2018, **9**, 4645.
33 L. Zhong, S. Jeong, S. Lee, T. L. H. Mai, J. Park, J. Park, W. Kim and C. Yang, *Chem. Commun.*, 2023, **59**, 12108–12111.
34 L. Zhong, S.-H. Kang, J. Oh, S. Jung, Y. Cho, G. Park, S. Lee, S.-J. Yoon, H. Park and C. Yang, *Adv. Funct. Mater.*, 2022, **32**, 2201080.
35 L. Zhong, Z. Sun, S. Lee, S. Jeong, S. Jung, Y. Cho, J. Park, J. Park, S.-J. Yoon and C. Yang, *Adv. Funct. Mater.*, 2023, 2305450.
36 J. Burschka, N. Pellet, S.-J. Moon, R. Humphry-Baker, P. Gao, M. K. Nazeeruddin and M. Grätzel, *Nature*, 2013, **499**, 316–319.
37 Y. Y. Kim, E. Y. Park, T.-Y. Yang, J. H. Noh, T. J. Shin, N. J. Jeon and J. Seo, *J. Mater. Chem. A*, 2018, **6**, 12447–12454.
38 L. Shen, P. Song, L. Zheng, L. Wang, X. Zhang, K. Liu, Y. Liang, W. Tian, Y. Luo, J. Qiu, C. Tian, L. Xie and Z. Wei, *Adv. Mater.*, 2023, **35**, 2301624.
39 S. Wang, H. Luo, Z. Gu, R. Zhao, L. Guo, N. Wang, Y. Lou, Q. Xu, S. Peng, Y. Zhang and Y. Song, *Adv. Funct. Mater.*, 2023, **33**, 2214834.
40 Z. Xiao, C. Bi, Y. Shao, Q. Dong, Q. Wang, Y. Yuan, C. Wang, Y. Gao and J. Huang, *Energy Environ. Sci.*, 2014, **7**, 2619–2623.
41 Q. Jiang, Z. Chu, P. Wang, X. Yang, H. Liu, Y. Wang, Z. Yin, J. Wu, X. Zhang and J. You, *Adv. Mater.*, 2017, **29**, 1703852.
42 S. M. Bouzzine, S. Bouzakraoui, M. Bouachrine and M. Hamidi, *J. Mol. Struct.: THEOCHEM*, 2005, **726**, 271–276.
43 J. Guo, J. Sun, L. Hu, S. Fang, X. Ling, X. Zhang, Y. Wang, H. Huang, C. Han, C. Cazorla, Y. Yang, D. Chu, T. Wu, J. Yuan and W. Ma, *Adv. Energy Mater.*, 2022, **12**, 2200537.
44 R. Wang, J. Xue, L. Meng, J.-W. Lee, Z. Zhao, P. Sun, L. Cai, T. Huang, Z. Wang, Z.-K. Wang, Y. Duan, J. L. Yang, S. Tan, Y. Yuan, Y. Huang and Y. Yang, *Joule*, 2019, **3**, 1464–1477.
45 Q. Cao, T. Wang, J. Yang, Y. Zhang, Y. Li, X. Pu, J. Zhao, H. Chen, X. Li, I. Tojiboyev, J. Chen, L. Etgar and X. Li, *Adv. Funct. Mater.*, 2022, **32**, 2201036.
46 Q. Yang, X. Liu, S. Yu, Z. Feng, L. Liang, W. Qin, Y. Wang, X. Hu, S. Chen, Z. Feng, G. Hou, K. Wu, X. Guo and C. Li, *Energy Environ. Sci.*, 2021, **14**, 6536–6545.
47 J. Hu, R. A. Kerner, I. Pelczer, B. P. Rand and J. Schwartz, *ACS Energy Lett.*, 2021, **6**, 2262–2267.
48 P. Boonmongkolras, D. Kim, Esra M. Alhabshi, I. Gereige and B. Shin, *RSC Adv.*, 2018, **8**, 21551–21557.
49 T. Liu, Y. Jiang, M. Qin, J. Liu, L. Sun, F. Qin, L. Hu, S. Xiong, X. Jiang, F. Jiang, P. Peng, S. Jin, X. Lu and Y. Zhou, *Nat. Commun.*, 2019, **10**, 878.
50 C. Luo, G. Zheng, F. Gao, X. Wang, Y. Zhao, X. Gao and Q. Zhao, *Joule*, 2022, **6**, 240–257.
51 M. E. O'Kane, J. A. Smith, R. C. Kilbride, E. L. K. Spooner, C. P. Duif, T. E. Catley, A. L. Washington, S. M. King, S. R. Parnell and A. J. Parnell, *Chem. Mater.*, 2022, **34**, 7232–7241.
52 C. Ran, W. Gao, N. Li, Y. Xia, Q. Li, Z. Wu, H. Zhou, Y. Chen, M. Wang and W. Huang, *ACS Energy Lett.*, 2019, **4**, 358–367.
53 Y. Wu, G. Xu, J. Xi, Y. Shen, X. Wu, X. Tang, J. Ding, H. Yang, Q. Cheng, Z. Chen, Y. Li and Y. Li, *Joule*, 2023, **7**, 398–415.
54 Y. Zhang, Y. Wang, X. Yang, L. Zhao, R. Su, J. Wu, D. Luo, S. Li, P. Chen, M. Yu, Q. Gong and R. Zhu, *Adv. Mater.*, 2022, **34**, 2107420.
55 H. Zhong, X. Liu, M. Liu, S. Yin, Z. Jia, G. Fu, S. Yang and W. Kong, *Nano Energy*, 2023, **105**, 108014.
56 P. M. Moreno-Romero, A. N. Corpus-Mendoza, M. A. Millán-Franco, C. A. Rodríguez-Castañeda, D. M. Torres-Herrera,

F. Liu and H. Hu, *J. Mater. Sci.: Mater. Electron.*, 2019, **30**, 17491–17503.
57 W. Shao, H. Wang, F. Ye, C. Wang, C. Wang, H. Cui, K. Dong, Y. Ge, T. Wang, W. Ke and G. Fang, *Energy Environ. Sci.*, 2023, **16**, 252–264.
58 Y. Zhao, H. Tan, H. Yuan, Z. Yang, J. Z. Fan, J. Kim, O. Voznyy, X. Gong, L. N. Quan, C. S. Tan, J. Hofkens, D. Yu, Q. Zhao and E. H. Sargent, *Nat. Commun.*, 2018, **9**, 1607.
59 T.-H. Kim, E. K. Jeon, Y. Ko, B. Y. Jang, B.-S. Kim and H.-K. Song, *J. Mater. Chem. A*, 2014, **2**, 7600–7605.
60 S. Song, S. J. Yang, W. Choi, H. Lee, W. Sung, C. Park and K. Cho, *Adv. Energy Mater.*, 2020, **10**, 2001759.
61 C. Zhu, X. Niu, Y. Fu, N. Li, C. Hu, Y. Chen, X. He, G. Na, P. Liu, H. Zai, Y. Ge, Y. Lu, X. Ke, Y. Bai, S. Yang, P. Chen, Y. Li, M. Sui, L. Zhang, H. Zhou and Q. Chen, *Nat. Commun.*, 2019, **10**, 815.
62 T. Yang, L. Gao, J. Lu, C. Ma, Y. Du, P. Wang, Z. Ding, S. Wang, P. Xu, D. Liu, H. Li, X. Chang, J. Fang, W. Tian, Y. Yang, S. Liu and K. Zhao, *Nat. Commun.*, 2023, **14**, 839.
63 L. Bi, Q. Fu, Z. Zeng, Y. Wang, F. R. Lin, Y. Cheng, H.-L. Yip, S. W. Tsang and A. K. Y. Jen, *J. Am. Chem. Soc.*, 2023, **145**, 5920–5929.
64 T. Huang, S. Tan, S. Nuryyeva, I. Yavuz, F. Babbe, Y. Zhao, M. Abdelsamie, M. H. Weber, R. Wang, K. N. Houk, C. M. Sutter-Fella and Y. Yang, *Sci. Adv.*, 2021, **7**, eabj1799.
65 K. Schötz and F. Panzer, *J. Phys. Chem. A*, 2021, **125**, 2209–2225.
66 Y.-C. Lin, M. Bettinelli and M. Karlsson, *Chem. Mater.*, 2019, **31**, 3851–3862.
67 M. Liu, Q. Wan, H. Wang, F. Carulli, X. Sun, W. Zheng, L. Kong, Q. Zhang, C. Zhang, Q. Zhang, S. Brovelli and L. Li, *Nat. Photonics*, 2021, **15**, 379–385.
68 D. Zhang, Y. Fu, H. Zhan, C. Zhao, X. Gao, C. Qin and L. Wang, *Light: Sci. Appl.*, 2022, **11**, 69.
69 F. Li, X. Deng, Z. Shi, S. Wu, Z. Zeng, D. Wang, Y. Li, F. Qi, Z. Zhang, Z. Yang, S.-H. Jang, F. R. Lin, S. W. Tsang, X.-K. Chen and A. K. Y. Jen, *Nat. Photonics*, 2023, **17**, 478–484.
70 Y. Li, Y. Duan, J. Feng, Y. Sun, K. Wang, H. Li, H. Wang, Z. Zang, H. Zhou, D. Xu, M. Wu, Y. Li, Z. Xie, Z. Liu, J. Huang, Y. Yao, Q. Peng, Q. Fan, N. Yuan, J. Ding, S. Liu and Z. Liu, *Angew. Chem., Int. Ed.*, 2024, **34**, e202410378.
71 L. Yang, H. Zhou, Y. Duan, M. Wu, K. He, Y. Li, D. Xu, H. Zou, S. Yang, Z. Fang, S. Liu and Z. Liu, *Adv. Mater.*, 2023, **35**, 2211545.
72 D. Glowienka and Y. Galagan, *Adv. Mater.*, 2022, **34**, 2105920.
73 S. Ryu, N. Y. Ha, Y. H. Ahn, J.-Y. Park and S. Lee, *Sci. Rep.*, 2021, **11**, 16781.
74 S. Ryu, D. C. Nguyen, N. Y. Ha, H. J. Park, Y. H. Ahn, J.-Y. Park and S. Lee, *Sci. Rep.*, 2019, **9**, 19846.
75 M. Sajedi Alvar, P. W. M. Blom and G.-J. A. H. Wetzelaer, *Nat. Commun.*, 2020, **11**, 4023.
76 Q. Jiang, L. Zhang, H. Wang, X. Yang, J. Meng, H. Liu, Z. Yin, J. Wu, X. Zhang and J. You, *Nat. Energy*, 2016, **2**, 16177.

